# Jovian Auroral Electron Precipitation Budget—A Statistical Analysis of Diffuse, Mono-Energetic, and Broadband Auroral Electron Distributions

**A. Salveter[1]** ID, **J. Saur[1]** ID, **G. Clark[2]** ID, and **B. H. Mauk[2]** ID

[1]Institute of Geophysics and Meteorology, University of Cologne, Cologne, Germany, [2]The Johns Hopkins University Applied Physics Laboratory, Laurel, MD, USA

**Abstract** Recent observations by the Juno spacecraft have shown that electrons contributing to Jupiter's main auroral emission appear to be frequently characterized by broadband electron distributions, but also less often mono-energetic electron distributions are observed as well. In this work, we quantitatively derive the occurrence rates of the various electron distributions contributing to Jupiter's aurora. We perform a statistical analysis of electrons measured by the JEDI-instrument within 30–1,200 keV from Juno's first 20 orbits. We determine the electron distributions, either pancake, field-aligned, mono-energetic, or broadband, through energy and pitch angles to associate various acceleration mechanisms. The statistical analysis shows that field-aligned accelerated electrons at magnetic latitudes greater than 76° are observed in 87.6% ± 7.2% of the intervals time averaged over the dipole L-shells according the main oval. Pancake distributions, indicating diffuse aurora, are prominent at smaller magnetic latitudes (<76°) with an occurrence rate of 86.2% ± 9.6%. Within the field-aligned electron distributions, we see broadband distributions 93.0% ± 3.8% of the time and a small fraction of isolated mono-energetic distribution structures 7.0% ± 3.8% of the time. Furthermore, these occurrence statistics coincide with the findings from our energy flux statistics regarding the electron distributions. Occurrence rates thus also characterize the overall energetics of the different distribution types. This study indicates that stochastic acceleration is dominating the auroral processes in contrast to Earth where the discrete aurora is dominating.

**Plain Language Summary** With the Juno spacecraft arriving in the magnetosphere of Jupiter, first flyby particle measurements have changed the knowledge about the developing process of Jupiter's intense aurora. The observations of auroral particles show a stochastic behavior rather than a preference for specific energy. Our statistical analysis of the first 20 flybys at Jupiter compares the occurrence of different particle distributions and highlights the importance of different generation theories for Jupiter's aurora. A generation via stochastic rather than mono-energetic behavior is deduced and supports previous observations.

## 1. Introduction

Jupiter's aurora is powered by a very unique magnetospheric environment strongly differing from the magnetosphere of Earth. The magnetosphere of Jupiter is mainly dominated by the planet's high rotation rate, strong magnetic field, and mass source Io, which ejects approximately 1 ton/s of plasma into the middle magnetosphere, rather than from a solar wind interaction (Bagenal & Delamere, 2011). However, expectations on auroral mechanisms were initially drawn from analogies with Earth, supported by remote optical observations of Jupiter's aurora (Clarke et al., 2002; Grodent et al., 2018; Kimura et al., 2015; Mauk et al., 2002; Tao et al., 2015) and equatorial in-situ measurements from the Galileo spacecraft and flyby missions such as the Voyagers (Bagenal et al., 2017). The Juno spacecraft—a Jupiter polar-orbiting mission launched in 2011 (Bolton et al., 2017)—has fundamentally changed our view of the Jovian aurora with the first-ever high-latitude in-situ measurements.

The dynamic of the magnetosphere is driven by the high rotation rate of Jupiter. The plasma sourced primarily by Io is picked up and accelerated to corotation speeds; however, corotation cannot be sustained at large distances. The radially outward moving plasma drives a current system associated with the breakdown of corotation that diverges and closes within the auroral ionosphere (Cowley & Bunce, 2001; Hill, 2001; Hill, 1979).

Knight (1973) introduced the theory of electric potentials along with the static current system to maintain the current density within the magnetosphere-ionosphere coupling, especially in low density regions at high latitudes.

Knight ([1973](#)) formulated a relation of the current density to the field-aligned potential, which accelerates particles to a specific energy. The acceleration process is therefore described as an electrostatic process, causing mono-energetic electron distributions. Standard particle calculations prior to the Juno mission were based on the Knight formula (Cowley & Bunce, [2001](#); Nichols & Cowley, [2004](#); Ray et al., [2010](#)).

The radial particle transport in the current sheet additionally causes small-scale magnetic field perturbations (Mauk & Saur, [2007](#); Saur et al., [2003](#); Tao et al., [2015](#)) as a consequence of discontinuous flux tube-driven transport. It is argued that local deviations of the force or stress balance of Jupiter's magnetosphere—ionosphere coupling cause small-scale magnetic field fluctuations to achieve stress-balance (Saur et al., [2018](#)). These magnetic-field perturbations then cascade to smaller scales as they are counter-interacting along magnetic field lines. When reaching the kinetic length and temporal scales, wave-particle interaction converts electromagnetic energy in the wave fields into particle energy. The processes can be summarized as locally stressed magnetic field lines. Stressed magnetic field lines lead to Alfvén waves, which transfer momentum between the magnetosphere and the ionosphere, causing stochastic acceleration (Saur et al., [2018](#)).

Both the large-scale electric current systems, as well as the small-scale magnetic field stresses, maximize in the middle magnetosphere, ranging from 15 to 20 $R_J$ up to approximately 50 $R_J$ (Cowley & Bunce, [2001](#); Hill, [2001](#); Saur et al., [2018](#)), and contribute to the main emission zone. Other regions such as the polar cap, here defined as the region poleward of the main emission zone, and satellite footprints are therefore not investigated. Magnetospheric processes in the middle magnetosphere are the root cause of the acceleration process of auroral particles, where the acceleration of particles is crucial to overcome magnetic mirroring forces to generate aurora. All acceleration processes, for example, stochastic and electrostatic, contribute to different electron energy distributions, which are well observed by the Juno spacecraft with the Jupiter Energetic-particle Detector Instrument (JEDI) at high electron energies ($25 - 1,200$ keV) (Mauk, Haggerty, Jaskulek, et al., [2017](#)) and Jovian Auroral Distributions Experiment (JADE) at low electron energies ($100$ eV $- 100$ keV) (McComas et al., [2017](#)) (for more information on Juno see Bagenal et al., [2017](#)).

Early observation of electrons along magnetic field lines connecting to the auroral regions by JEDI showed that the electron energy spectra are broadband, not structured in energy, and with a shallow slope (i.e., hard) extending beyond $\approx 800$ keV (Mauk et al., [2017b](#); Allegrini et al., [2017](#)). Regions with upward loss cones indicate diffuse aurora, either seen by Ultraviolet Spectrograph (UVS), JEDI, and JADE (Allegrini et al., [2017](#); Li et al., [2017](#)). Additionally, no large magnetic perturbations ($\leq 1\%$) due to field-aligned currents associated with the auroral zones were observed, suggesting no potential drops as the primary auroral driver (Connerney et al., [2017](#); Kotsiaros et al., [2019](#)). Later measurements then observed isolated mono-energetic distributions from 1.4 to 2.9 $R_J$ associated with electric potentials up to 400 keV, but still with less energy flux than from stochastic characteristics (Clark, Mauk, Paranicas, et al., [2017](#); Ebert et al., [2017](#); Mauk et al., [2017a](#)). Several other mono-energetic distributions over the main emission zone have been observed, but the most intense auroras with high energy flux are still generated by stochastic processes (Mauk et al., [2017b](#)). The observations indicate no evidence for one clear assignable acceleration process, rather a composition or even a transition between broadband and mono-energetic distributions (Mauk et al., [2018](#)).

Comparison with other Juno instruments has shown similar conclusions, as by comparison with UVS images. Gérard et al. ([2019](#)) concluded observed polar emissions are even more than an order of magnitude brighter than expected from downward energy flux calculations. However, upward energy flux calculations show sufficient energy flux, indicating a bidirectional broadband electron acceleration below Juno's altitude (Ebert et al., [2019](#)). Upgoing electron beams also showed evidence of whistler-mode wave emission driven by downward electric potentials, but mainly within the polar cap (Elliott, Gurnett, Kurth, Clark, et al., [2018](#); Elliott, Gurnett, Kurth, Mauk, et al., [2018](#); Tetrick et al., [2017](#)). A comparison of main aurora particle features and plasma waves that accompany the features is diagnosed with the Waves instrument by Kurth et al. ([2018](#)), where the importance of whistler waves, as well as Alfvén waves, is highlighted. A separation of the auroral zones has been accomplished by Mauk et al. ([2020](#)), where three distinct zones are introduced, diffuse aurora (DifA), Zone I (ZI), and Zone II (ZII). The DifA primarily shows empty loss cones, with a small enhancement of energy flux in the downward rather than in the upward direction. Zone ZI and ZII are classified by filled loss cones, respectively, in either downward or upward direction, characterized by a dominating energy flux within the loss cones (Mauk et al., [2020](#)). The two Zones, ZI and ZII, are associated with upward and downward currents, where both Zones are dominated by broadband distributions with some mono-energetic features.

In the case of Earth's aurora, mono-energetic electrons contribute a larger energy flux than broadband accelerated electrons (Newell et al., 2009). In contrast, Juno's observations reveal that broadband statistically accelerated electrons may be dominant for Jupiter's aurora (Mauk et al., 2017b) and might play an important role in Saturn's magnetosphere as well (Saur et al., 2006). What has been missing so far is a quantitative study statistically analyzing the occurrence rates to quantify the contribution of different energy distributions and associated acceleration processes to the Jovian aurora. Such a study is now possible for Jupiter as the Juno mission acquired sufficient observation to perform a statistical analysis. Our study compares the occurrence of different auroral precipitation types such as diffuse, mono-energetic, and broadband aurora to investigate the occurrence of filamentation as a driving part for particle acceleration. Properties such as particle distributions and energy fluxes are used to classify regions into the corresponding precipitation types, as introduced by Mauk et al. (2020). This statistical study is based on the times when Juno's location magnetically maps to the main emission zones. We omit auroral processes in the polar cap and satellite regions. Several conditions to the time windows selection are therefore introduced in Section 2, followed by the classification of precipitation types based on Mauk et al. (2020).

## 2. Data and Classification Scheme

In-situ observations of electron and ion distributions with the Juno spacecraft are performed by JEDI and its complement at lower energies, JADE (Bagenal et al., 2017, for more information on Juno). In the following JEDI data will be used to investigate the precipitation of energetic electrons within an energy range from 25 to 1,200 keV (Mauk et al., 2017). The JEDI instruments consist of 18 solid state detectors (SSDs) to measure single electron rates in different look directions at the same time. Six SSDs are arranged in a 160° fan for each of three instruments, together covering a nearly 360° field of view (Mauk et al., 2017). To characterize the acceleration process, we organize the electrons as a function of local pitch angle—the angle between the particle velocity and magnetic field vector measured by Juno's magnetometer (Connerney et al., 2017). The instrument's alignment with the spacecraft plane allows full pitch angle coverage when the magnetic field line is contained within the plane roughly perpendicular to the spacecraft spin vector. In Section 2.3, we will introduce a condition for reasonable data selection based on good pitch angle coverage. The SSDs measure for 0.25 s every 0.5 s. Even small structures of a few hundred kilometers are resolvable, because the spacecraft velocity is ≈50 km/s near Jupiter. JEDIs pitch angle coverage is decimated as Juno's orbit evolves and relies more on the S180 sensor that is mounted perpendicular to Juno's spin plane. The consequence is that instead of near instantaneous pitch angle coverage in the earlier orbits, full pitch angle coverage is built up over the 30 s spacecraft spin period. The smallest resolvable size close to Jupiter is then approximately 1,500 km, broader than many auroral features. The statistical study is confined to the first 20 perijoves. Good pitch angle coverage will be additionally tested based on comparison to the local loss cone size, as further described in Section 2.3, with the loss cone size defined as shown in Section 2.2.

The observed electron counts need to be rigorously evaluated on signal-to-noise ratio, as electrons can scatter on foils, grids, and other internal surfaces and stimulate unintended SSDs as further described in Section 2.4. The resulting adequately resolved times are processed by a classification in precipitation types considering the electron pitch angle and energy distributions, as further explained in Section 2.5.

### 2.1. Emission Zone

The subject of our investigation of auroral acceleration mechanisms is the main emission zone. The observation of associated precipitating auroral electrons is restricted to small radial distances and along magnetic field-lines mapping to the main emission zone. To ensure the observation of accelerated particles, the spacecraft needs to be below expected heights of acceleration and within a radial distance where the geometric loss cone is large enough that the loss cone distribution is resolved by JEDI's angular field of view (Clark et al., 2018). We, therefore, select the data by a radial distance of 1.2–2.5 $R_J$ (Clark et al., 2018; Ebert et al., 2017). We assume the shape of Jupiter to be a sphere with a radius of 71,492 km as the JPL navigation team proposes throughout all Juno activities (Bagenal et al., 2017). Note that the polar radius of Jupiter is much less (66,854 km) because of the high rotation rate of the planet, described by a flattening of 1/15.4 of Jupiter's surface (Bagenal et al., 2017). Furthermore, the spacecraft footprint in the atmosphere should locate in the expected zones of main auroral emission. The mapping from the spacecraft onto the atmosphere can be processed by the combination of the

Juno Reference Model through Perijove 9 (JRM09) (Connerney et al., 2018) with the current sheet model (CAN) (Connerney, 1981).

To describe the position of the Juno measurements the M-shell model (JRM09 and current sheet model) has been used in the literature with M-shells which range up to 100. However, the current sheet model is defined only within 5–50 $R_J$ and thus cannot be used for values larger than 50, where it leads to spurious values (see Text S1 in Supporting Information S1). Since the purpose of this paper is not the mapping of the observed electrons into the magnetosphere, but a characterization of the electrons near Jupiter, we use coordinates which are as model-independent as possible. We will therefore use magnetic latitude $\theta_M$, which is additionally related to L-shell. However, we point out that L-shell does not provide an accurate mapping into the equatorial region of Jupiter's magnetosphere in particular for large distance starting at 20 to 30 $R_J$. Therefore, we will use in this work magnetic latitude as the primary coordinate to describe the position of the measurements and will show in addition the L-shell value as a lower limit for the real L-shell crossing. We will use the dipole L-shell boundaries from 8 to 50 Jovian radii to include observations mapping to the Hubble Space Telescope (HST) main auroral oval (Bonfond, 2012), as shown in supporting material Figure S2 in Supporting Information S1.

### 2.2. Loss Cone Calculations

High energy particles precipitate into the atmosphere to excite atoms generating auroral emission. This is possible when the relation of parallel velocity to orthogonal velocity, in the frame of the magnetic field lines, is sufficiently large to overcome mirroring forces arising from the invariant magnetic moment, constant energy of motion, and converging magnetic field lines (Baumjohann & Treumann, 1997). Those precipitating particles, therefore, possess a smaller pitch angle (PA) than the maximal angle of $\alpha_c$ the loss cone (LC) angle. All particles inside the loss cone therefore contribute to the precipitating particles generating discrete aurora. Particles outside of the loss cone cannot overcome mirroring forces and are trapped above the atmosphere, bouncing between both hemispheres.

The definition of the loss cone

$$\alpha = \sin^{-1}\left(\sqrt{\frac{B_{sc}}{B_{atm}}}\right) \tag{1}$$

depends on the relation of magnetic field strength at the spacecraft $B_{sc}$ and the magnetic field strength at the atmosphere $B_{atm}$ (Baumjohann & Treumann, 1997). The magnetic field strength at the spacecraft is measured with the onboard fluxgate magnetometer. The magnetic field strength of Juno's footprint at the atmosphere is primarily computed using the JRM09 (Connerney et al., 2018) taking the high influence of the higher magnetic moments at small radial distances into account, as well as using the current sheet model (Connerney, 1981) whose influence is negligibly small at small radial distances. The top atmospheric layer, the exosphere, does not have a specific upper boundary, but several studies and models suggest an upper boundary of approximately 400 km above the 1 bar level (Gérard et al., 2014; Seiff et al., 1998), where the 1 bar level is computed as the dynamically flattened (1/15.4) surface of Jupiter (Connerney et al., 2018).

### 2.3. Pitch Angle Coverage

The resolution of the loss cone strongly depends on the pitch angle coverage which is mostly sufficient when the spacecraft rotation axis is nearly perpendicular to the magnetic field line. Restrictions to the mounting of the sensors and the alignment of the spacecraft cannot provide the full field-aligned pitch angular coverage to 0° and 180°. For some times the maximal and minimal covered pitch angle from all detectors does not reach into the loss cone. A sufficient loss cone coverage is thus provided when these boundary pitch angles lie within the identified loss cone from Section 2.2. To neglect the temporal influence of the spacecraft spin, we calculate the mean of the pitch angle boundary with a rolling window of 30 s width corresponding to the spacecraft spin period. This ensures that the spacecraft orientation provides at least a loss cone coverage over at least 50% of the time interval.
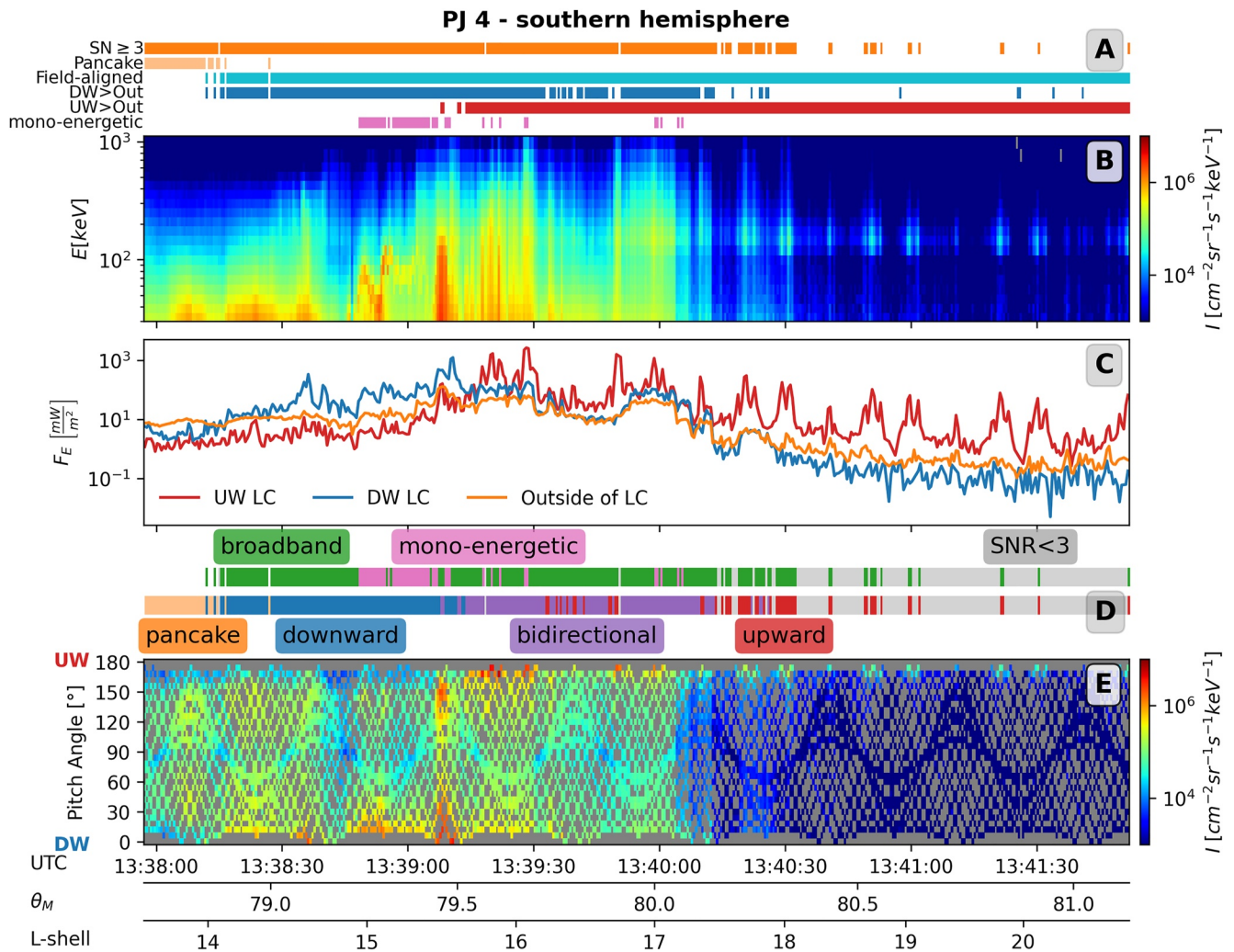
**Figure 1.** Classification of Juno's fourth southern hemispheric flyby over the main emission zone. Panels (b) and (e) show energy-time and pitch angle-time spectrograms of intensities, respectively, measured by the JEDI instrument. The "speckled" pattern of the pitch angle distribution results from incomplete pitch angle coverage, where the gray color corresponds to absent measurements. The energy flux calculated by Equation 2 is shown in (c) for the upward (UW) and downward (DW) loss cone, as well as outside of the loss cone (Out). Panels (a) shows color-coded the status of the applied criteria tagged on the left side and (d) shows the resulting classification into the type of the energy distribution, that is, broadband (green) or mono-energetic (pink), and the various types of pitch angle distributions, that is, pancake (orange), downward (blue), bidirectional (purple), and upward (red). The JRM09 L-shell, and the corresponding magnetic latitude at $r = R_J$ are also provided.

### 2.4. Signal to Noise

We only address times when a sufficient amount of electron counts has been observed and an appropriate signal-to-noise ratio is obtained. The electron counts are measured by the SSDs which detect particles coming through the sensor head over a predefined time interval. As the detectors measure finite numbers of counts over finite time intervals, the uncertainties or the noise arises from the independence of the events, rather than from a lack of precision in the measuring instrument (Bevington et al., 1993; Mauk et al., 2017). We therefore consider the measurements as Poisson-distributed events with the associated statistical uncertainties. If the counts per accumulation are small, then they might not contribute to a sufficient signal-to-noise ratio (SNR) and thus cannot be used to derive auroral fluxes. Relative uncertainties of Poisson-distributed counts are high when count rates are small, described by the signal-to-noise ratio $SNR = \sqrt{N}$, with $N$ counts in the time interval $\Delta t$ (Bevington et al., 1993). To neglect weak intensity regions from statistics, we only address times with a signal-to-noise ratio of at least 3, resembling a relative error of 33%, and a measurement of at least nine counts for the mean of one energy channel. This threshold works fine with by-eye-inspections as shown in Figure 1, where the low intensity

region after 13:40:30, panel b, has an insufficient SNR to be considered as signal (orange beam in panel a). The threshold has shown that all important features as known from previous main emission observations (e.g., Mauk et al., 2017b; Clark, Mauk, Haggerty, et al., 2017) has been included. Figure 1 shows a flyby over the northern polar region during Juno's fourth perijove, where the orange bar within part A of the figure marks regions with sufficient SNR including all significant beam structures as observed in the energy (part b) and pitch angle (part e) spectra.

### 2.5. Classification

The classification of types of electron distributions is processed by two steps. The first step is used to distinguish between field-aligned and trapped particles by considering pitch angle distributions, as described in Section 2.5.1. The second step is used to distinguish between mono-energetic and broadband distributions, by observing the intensity-energy spectra on broadband and mono-energetic structures, as described in Section 2.5.2. The two-step classification is applied to time intervals chosen under the conditions summarized in previous subsections.

#### 2.5.1. Pancake and Field-Aligned

Plasma particles contributing to the aurora are characterized by field-aligned motion, confined to the downward loss cone. Hence, particles within field-aligned distributions can precipitate into the atmosphere and generate aurora. Pancake distributions correspond to a dominant fraction of particles outside of the loss cone, which are not likely to precipitate into the atmosphere. Trapped particles can be scattered back into the loss cone and contribute to diffuse aurora, an unstructured and semi-permanent type of aurora. The diffuse aurora mainly results from wave-induced scattering processes, whereas discrete aurora results from particle acceleration along the magnetic field-lines at low-altitudes, showing sharply defined and time-variable structures (Mauk & Bagenal, 2012; Ni et al., 2016).

To determine the corresponding distributions for each timestep, we compare energy fluxes inside the loss cone, for upward or downward direction, with the energy flux outside of the loss cones, as introduced by Mauk et al. (2020). We filter the intensities for every sensor by the corresponding pitch angles and perform the sum

$$\pi \cdot \sum_n I_n(\alpha) \, E_n \cdot \Delta E \qquad (2)$$

where $n$ stands for each energy channel, $E_n$ is the central energy of the channel, $\Delta E_n$ is the energy bandpass of the channel, and $I_n$ is the measured intensity of the channel $n$ (Mauk et al., 2017b). The projection of the loss cone onto the atmosphere with the area-projection-weighted size $\pi$ is applied while assuming that the loss cone is fully populated. The resulting fluxes correspond to the energy fluxes at Jupiter's surface if we assume that there is no retarding electron potential comparable to the energies involved (Mauk et al., 2017b). The electron population outside of the loss cone does not reach the atmosphere. The one-directional energy flux at spacecraft altitude is given by the same expression as in Equation 2 under the assumption that the loss cone angle $\alpha_L \ll \pi/2$. At spacecraft altitude the local one-directional energy flux within the loss cone and outside of the loss cone scale by $\tan^2\alpha_L$ for similar intensities inside and outside of $\alpha_L$. In this work, we compare the downward going energy fluxes at the surface of Jupiter, which is responsible for the aurora, and the energy fluxes outside of the loss cone at spacecraft altitude and therefore use Equation 2 in both cases.

The resulting energy fluxes are shown in Figure 1c for Juno's fourth perijove. The different regions dominated by downward or upward energy flux are shown in Figure 1a. Pancake distributions are recognized in regions where neither the downward or upward energy flux are greater than outside of the loss cones, as defined by Mauk et al. (2020). All other times, when neither the downward nor the upward energy flux is greater than outside the loss cone, are defined as field-aligned distributions. The classification scheme is applied to every timestamp of the raw data with the highest temporal resolution of 0.5 s. The results from the classification are shown in Figure 1d with pancake or field-aligned distributions, where the field-aligned distributions are subdivided into mono-energetic and broadband distributions, as further described in Section 2.5.2. Field-aligned distributions are furthermore subdivided in upward, downward, and bidirectional regions, where either the upward or downward energy flux is greater than outside of the loss cones or both directions are greater resulting in a bidirectional distribution. Additionally, Zone I and Zone II as introduced by Mauk et al. (2020), are classified corresponding to either region of dominating downward or upward energy flux, respectively.
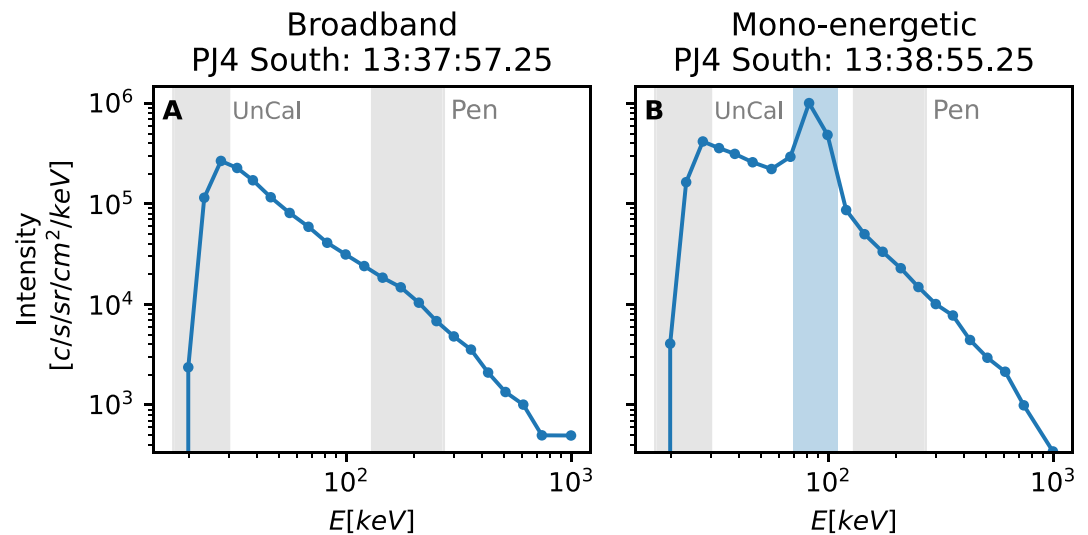
**Figure 2.** Example energy spectra for two selected times of Juno's fourth perijove in the southern hemisphere. Panel (a) shows a typical broadband distribution, (b) shows a mono-energetic distribution with a peak around 100 keV, marked by the blue zone. Peaks within the gray zone marked by "pen" for penetration would indicate high electron energies of >10 MeV penetrating the sensor head and leaving behind contamination at roughly 160 keV by secondary electrons. The gray zone marked as "Uncal" is yet not accounted for with the calibration process of the efficiencies.

### 2.5.2. Broad and Mono-Energetic Energy Distributions

Field-aligned particles show enhanced energy fluxes within at least one loss cone direction, upward and downward, and thus show evidence of highly energetic or dense particle distribution contributing to a specific acceleration process. The signatures of electrostatic and stochastic acceleration are used to define the respective classification into broadband and mono-energetic structures for each timestep's energy distribution. Broadband structures show a long tail in the energy distribution with strong intensities even exceeding into high energies. Broadband distributions can be similar to kappa distributions, which are based on Maxwellian distributions but provide a high-velocity tail with a power-law distribution (Baumjohann & Treumann, 1997). A typical broadband distribution is shown in Figure 2a for a selected timestamp of Juno's fourth southern perijove. The energy spectrum is limited to the measuring range of JEDI and the efficiency of the channels. However, distinct from a broadband distribution is the continuous decrease of the intensities with high energies. The rising intensities with increasing energy at low energies result from increasing efficiencies within each channel that are not yet accounted for in the calibration process, as marked by "Uncal" in Figure 2. The channels are properly calibrated above 30 keV. Low energy channels are thus excluded from the energy distribution classification. Channels between 130 and 270 keV, as marked by "Pen" in Figure 2, are additionally excluded due to the minimum ionizing effect of very high energetic electrons. Electrons in the MeV-class can fully penetrate the SSDs and leave a fraction of their full energy behind. This minimum ionizing energy for 0.5 mm SSDs at JEDI peaks at 160 keV (Mauk et al., 2018; Text S1 in Supporting Information S1). Enhanced intensities around this minimum ionizing energy indicate very energetic electron distributions extending into mega electron volt ranges and do not contribute to the electron's energy distribution. Intensities within remaining energy channels need to decrease continuously with increasing energy to define regions with broadband acceleration, where the mean intensity from all solid state detectors is used.

The determination of mono-energetic structures with JEDI are limited by the observable energy range, the altitude of Juno's flyby as well as the impact of penetrating particles on the electron distribution. Penetrating particles can leave behind high intensities similar to mono-energetic structures but mark highly energetic particles outside of the JEDI measuring range. But energy distributions with a high impact by highly energetic particles penetrating into the detector are not expected to show inverted-V structures in the JEDI energy range, as Mauk et al. (2018) (Supporting Information S1) stated that energy distributions with mono-energetic structures observed by JEDI are rarely accompanied by a minimum ionizing peak due to a high energy tail.
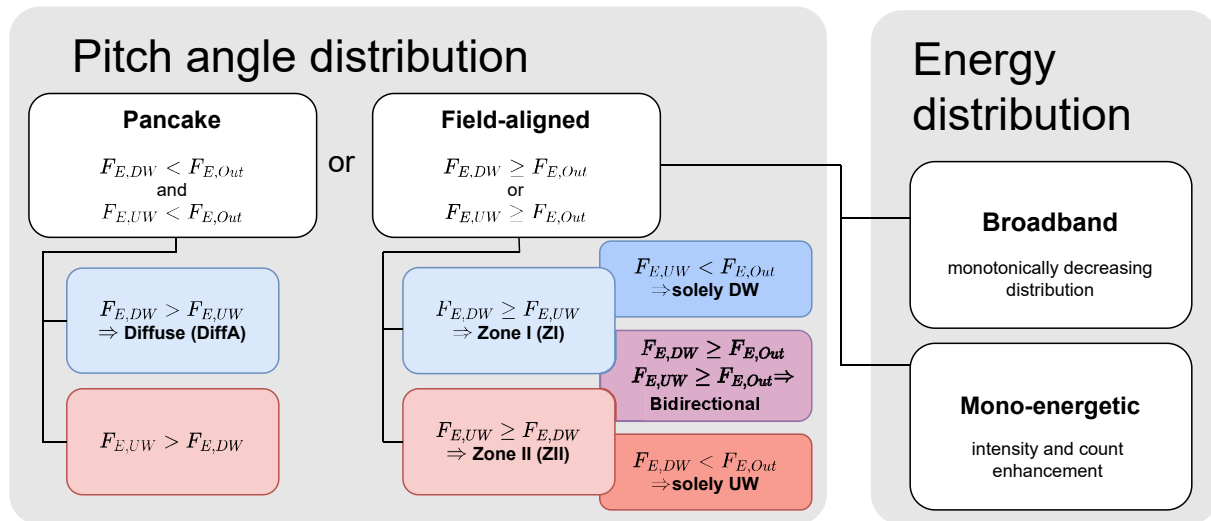
**Figure 3.** Classification scheme based on pitch angle and energy distribution analysis. The classification is based on energy flux $F_E$ comparisons for electrons outside the loss cone (Out) and electrons inside the loss cone, either in the upward (UW) or downward (DW) direction.

However, we define an energy distribution as a mono-energetic distribution when at least one energy channel, outside of the minimum ionizing energy range, peaks in intensity throughout the monotonically decreasing spectra. To neglect the impact of noise on the distribution classification, the enhancement needs to occur in both intensities and counts. The intensity enhancement is thereby not restricted, but the counts need to increase by at least nine counts to reduce the influence of noise, as further described in Section 2.4. An underestimation of mono-energetic structures might arise, as downward accelerated electrons from potentials below the spacecraft cannot be observed, but are expected, as deduced from upward accelerated protons (Szalay et al., 2021).

The energy distributions are summed over all SSDs and thus all pitch angles. A further classification can also be accomplished by filtering the intensities for the upward and downward loss cone and outside of the loss cone. An example of mono-energetic signatures is shown in Figure 2. Figure 2b shows a significant and clear intensity enhancement at 13:38:55 around roughly 100 keV identifying signatures related to mono-energetic acceleration processes (Mauk et al., 2017a). The corresponding regions are marked in Figures 1a, 1d. The classification of broadband or mono-energetic completes the classification scheme for mono-energetic, broadband, and diffuse aurora as summarized in Figure 3.

## 3. Results

The application of the classification scheme is only applied to times when Juno is located over the main emission zone, selected by restrictions on the distance $r$ and dipole L-shell parameter $L$, as described in Section 2. An overview of the spacecraft's location over the poles is given in Figure 4a. Good pitch angle coverage is only provided for the first 20 flybys over the main emission zone, and verified by loss cone calculations depending on the local magnetic field strength (see Section 2). The resulting time spans with adequate data coverage thus strongly vary in duration while considering all restrictions. Some perijoves only resolve the desired region for less than a minute, some others for more than 10 min. An overview of the resulting length of applicable data is shown in Figure 4b. The number of flybys in the southern hemisphere is very limited, as the spacecraft is farther away from Jupiter. A sufficient signal-to-noise ratio also reduces the useable times. Figure 4b shows the resulting times in red. The resulting times are used to apply the classification scheme, as described in Section 2.5, on the pitch angle distribution as well as on the energy distribution. Both together are used to define the regions of broadband, mono-energetic, and diffuse aurora.

The classification via pitch angle distribution shows that the greatest amount of observed particles with pancake distributions is confined to magnetic latitudes less than 76° corresponding to an L-shell of 17, where they contribute by 86.2% ± 9.6%, as shown in Figures 5a and 5b. This is not surprising, as diffuse aurora is associated with the scattering of magnetically trapped particles in the radiation zone at low altitudes.
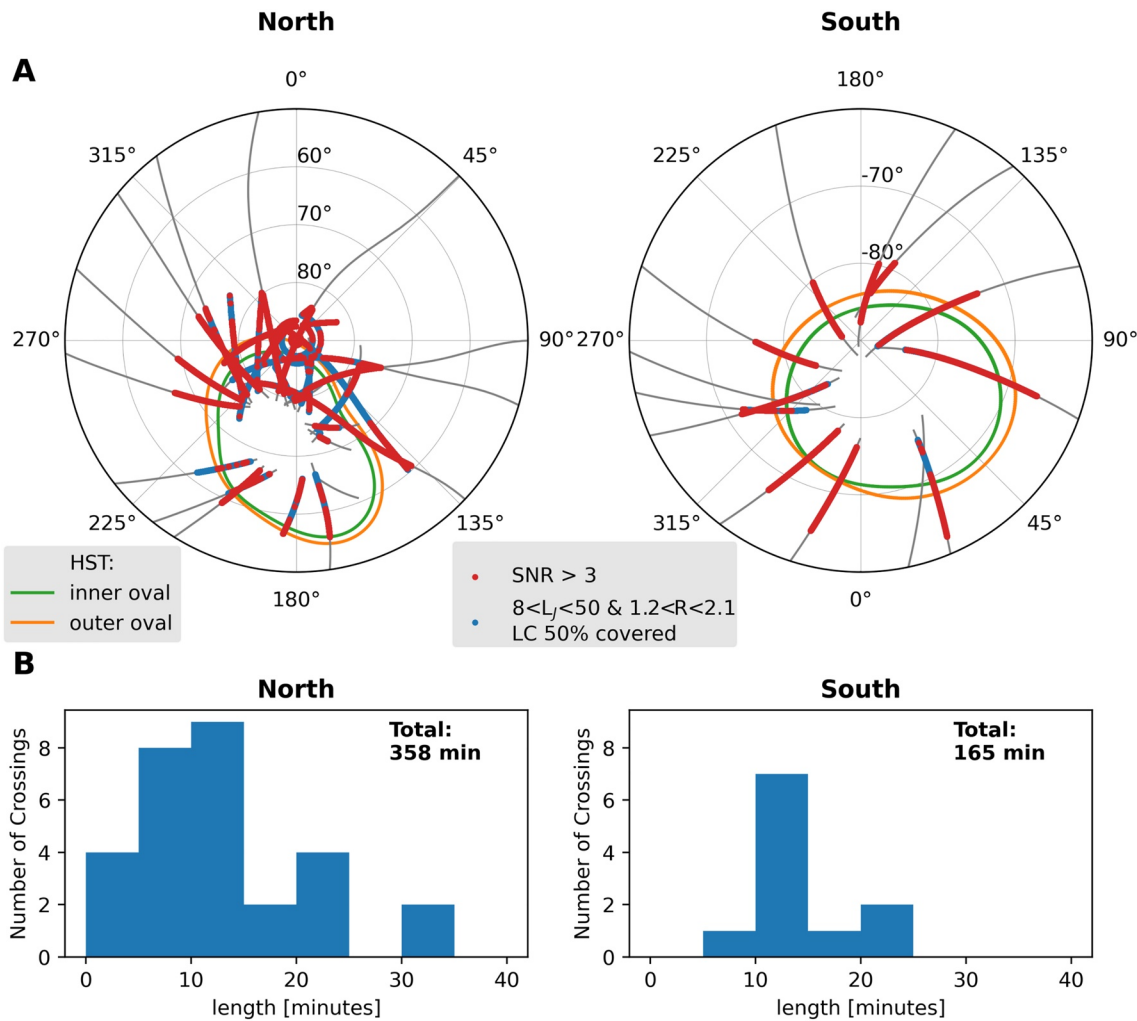
**Figure 4.** Part (a) Overview of the processed data over the main emission zone in SysIII coordinates. The gray lines show the perijoves of the first 20 flybys, where the blue points mark regions above the main emission zone. The red points overlay the blue points and show the fraction over the main emission zone which provides a sufficient signal-to-noise ratio of at least 3. Both criteria, blue and red, need to be fulfilled for the distribution to contribute to the statistical analysis. The averaged HST oval from Bonfond (2012) is added by the green and orange lines. Part (b) Histogram of the spacecrafts crossing duration's over the main emission zone, meeting the blue criteria, for all perijoves.

Field-aligned particle distributions increase in occurrence with increasing magnetic latitude and dominate with a fraction of 87.6% $\pm$ 7.2% for magnetic latitudes greater than 76°, with the mean and standard deviation (SD) calculated from their occurrence throughout the L-shell bins. These studies, however, do only represent the instrument's observation times. A complete overview covering the complete main emission zone is not feasible and our studies are biased by the supported number of measurements within the different magnetic latitudes.

The results from the classification via energy spectra into either broadband or mono-energetic distributions are shown in Figure 6, again as a function of the magnetic latitude. Mono-energetic distributions are less frequent than broadband distributions throughout all perijoves. Most of the mono-energetic structures are observable on very small time scales, but some emerge for a long duration even with inverted-V structures as seen in perijove 4 (Figure 1). But still, broadband distributions are dominating the field-aligned distributions over 93.0% of the time, where mono-energetic distributions contribute with a small fraction of 7.0% averaged over all dipole L-shells, both with a SD of 3.8% from Figure 6b.

The statistical study is applied to the highest temporal resolution of 0.5 s. However, a constant pitch-angle coverage, due to the SSDs separation, can only be obtained with a bin size of at least 5 s (Mauk et al., 2020). We, therefore, compare the results of our classification scheme based on 0.5 and 5 s bin size. The contribution of
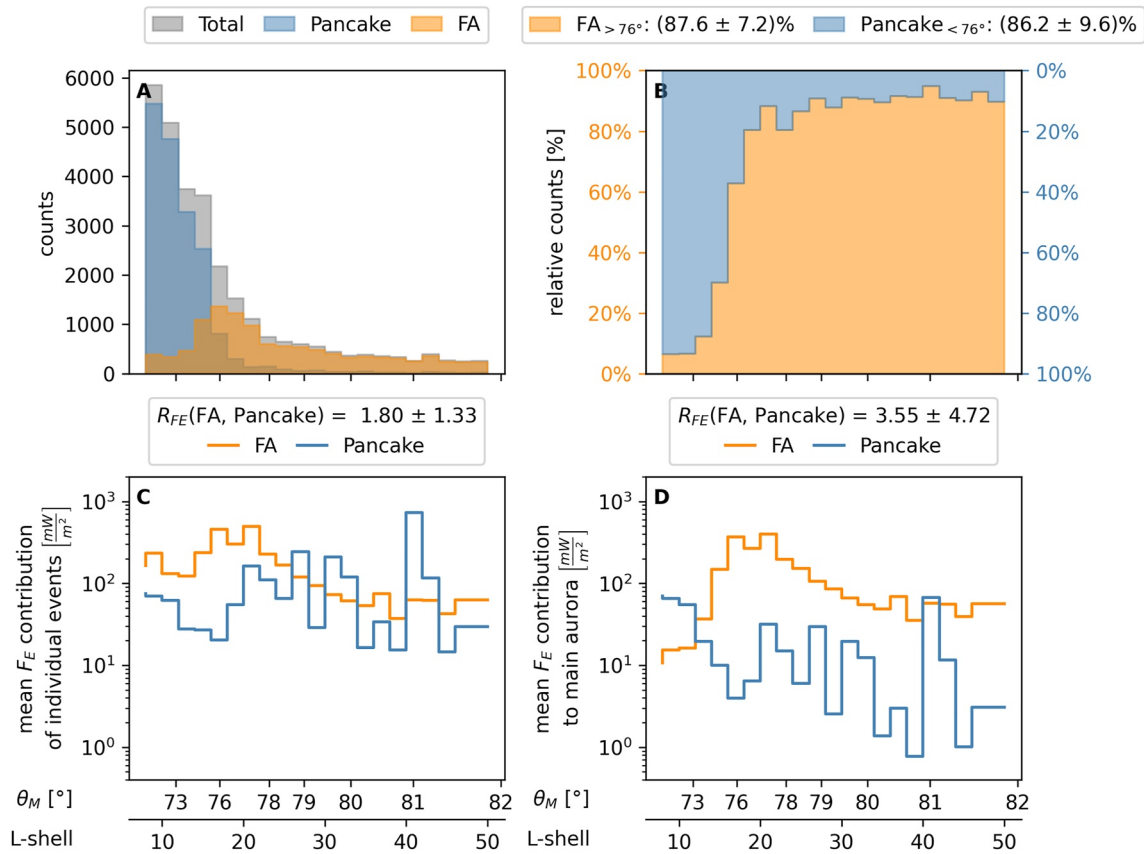
**Figure 5.** Histogram of field-aligned (FA) and pancake distributions as a function of the magnetic latitude, distributed/organized by the dipole L-shell. Part (a) shows the absolute number of observations in the corresponding dipole L-shell range. The stacked part of both plots shows the absolute counts of observations, where one count resembles one 0.5 s measurement. Part (b) shows the counts relative to the total number of observed distributions. Panels (c) and (d) show the mean energy flux for the classified distributions for the individual events and over the main emission zone, respectively.

field-aligned and pancake distributions differed by 0.5% and the contribution of broadband and mono-energetic distributions showed a difference of 1.25%. The choice of the bin size between 0.5 and 5 s thus only shows a minor influence, especially while comparing to the SDs of the contributions.

The statistical results are based on comparing the number of 0.5 s measurements identified within each classification category. The statistical analysis can also be performed on the mean energy flux $f_E$. Let us denote the energy flux within an 0.5 s event at time $t_k$ within a L-shell bin $L_j$ as $f_E^i(t_k, L_J)$, where $i = 0$ stands for field aligned, $i = 1$ for pancake, $i = 2$ for the field aligned subclass broadband, and $i = 3$ for field-aligned subclass mono-energetic events. The average energy flux of individual events of type $i$ within $L_j$ is given by

$$F_{E,individual}^i(L_j) = \frac{1}{N_k^i(L_j)} \sum_k^{N_k^i(L_j)} f_E^i(t_k, L_j) \tag{3}$$

with $N_k^i(L_j)$ the number of events of type $i$ within L-shell bin $L_j$. The overall average energy flux deposited into Jupiter's auroral region is given by

$$F_{E,abs}^i(L_j) = \sum_k^{N_k^i(L_j)} f_E^i(t_k, L_j). \tag{4}$$

With an average energy flux $F_E$ (i.e., Equation 3 or 4) we can define the average ratio of the energy flux between types $i = 0$ and $i = 1$ (field-aligned vs. pancake) or types $i = 2$ and $i = 3$ (broadband vs. mono-energetic) within individual events $R(F_{E,individual})$ and within the auroral region $R(F_{E,abs})$. The following equations describe the
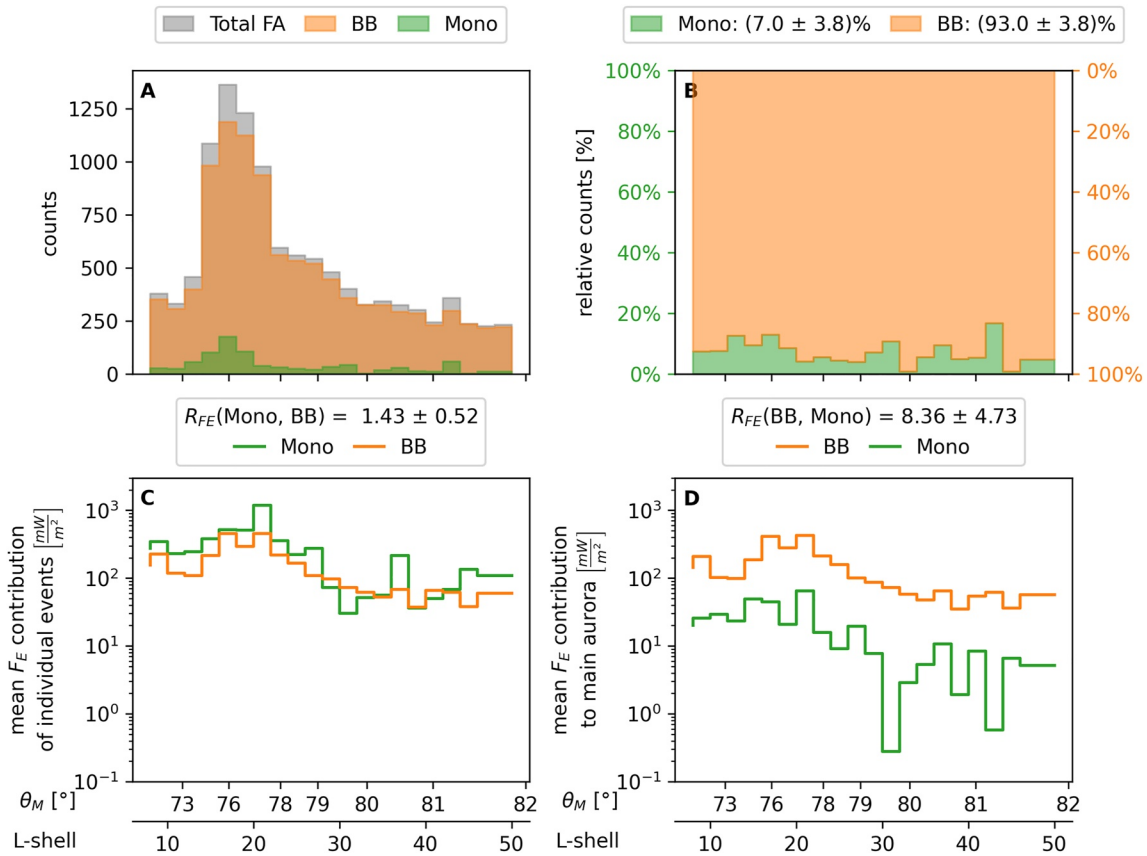
**Figure 6.** Histogram of broadband (BB) and mono-energetic distributions (mono) for field-aligned particles as a function of the magnetic latitude, organized by the dipole L-shell. Part (a) shows the absolute counts of classified distributions in the corresponding dipole L-shell range. The stacked part of all plots shows the absolute counts of observations, where one count resembles one 0.5 s measurement. Part (b) shows the counts relative to the total number of observed distributions. Panels (c) and (d) show the mean energy flux for the classified distributions for the individual events and over the main emission zone, respectively.

ratios between distribution types $i = 2$ and 3, but the ratio of energy fluxes between distribution types $i = 0$ and 1 are defined, similarly. The average ratio of the energy fluxes is given by

$$R(F_E) = \sum_j^{N_j} \frac{F_E^2(L_j)}{F_E^2(L_j) + F_E^3(L_j)} \bigg/ \sum_j^{N_j} \frac{F_E^3(L_j)}{F_E^2(L_j) + F_E^3(L_j)} , \tag{5}$$

calculated with the energy flux of individual events $R(F_{E,\text{individual}})$ and the energy flux within the auroral region $R(F_{E,\text{abs}})$. The latter takes into account the higher occurrence numbers of broadband events $N_k^2$ compared to mono-energetic events $N_k^3$.

The energy flux contribution of field-aligned and pancake distributions shows similar statistics compared to the relative counts, as seen in Figure 5b. Only magnetic latitudes of less than 79° show significant changes. Considering the average energy flux of individual events, we find that the field-aligned distributions exhibit slightly larger energy fluxes than pancake distributions (Figure 5c). If we compare the overall energy flux to the main aurora which additionally considers the higher occurrence of the field-aligned electrons compared to the pancake distributions (Figure 5b), then we find that the field-aligned energy fluxes significantly dominate. The overall energy flux of the field-aligned distribution is $3.55 \pm 4.72$ times larger compared to the pancake distribution. Only latitudes of less than 76° show a dominant energy flux contribution by pancake distributions. Some inaccuracies in the determination of these precipitation energy fluxes are governed by the determination of the loss cone size, because of the smearing of the energy flux response due to the finite width of the instrument view cone. This causes an uncertainty in characterizing the energy fluxes associated with trapped pancake distributions.
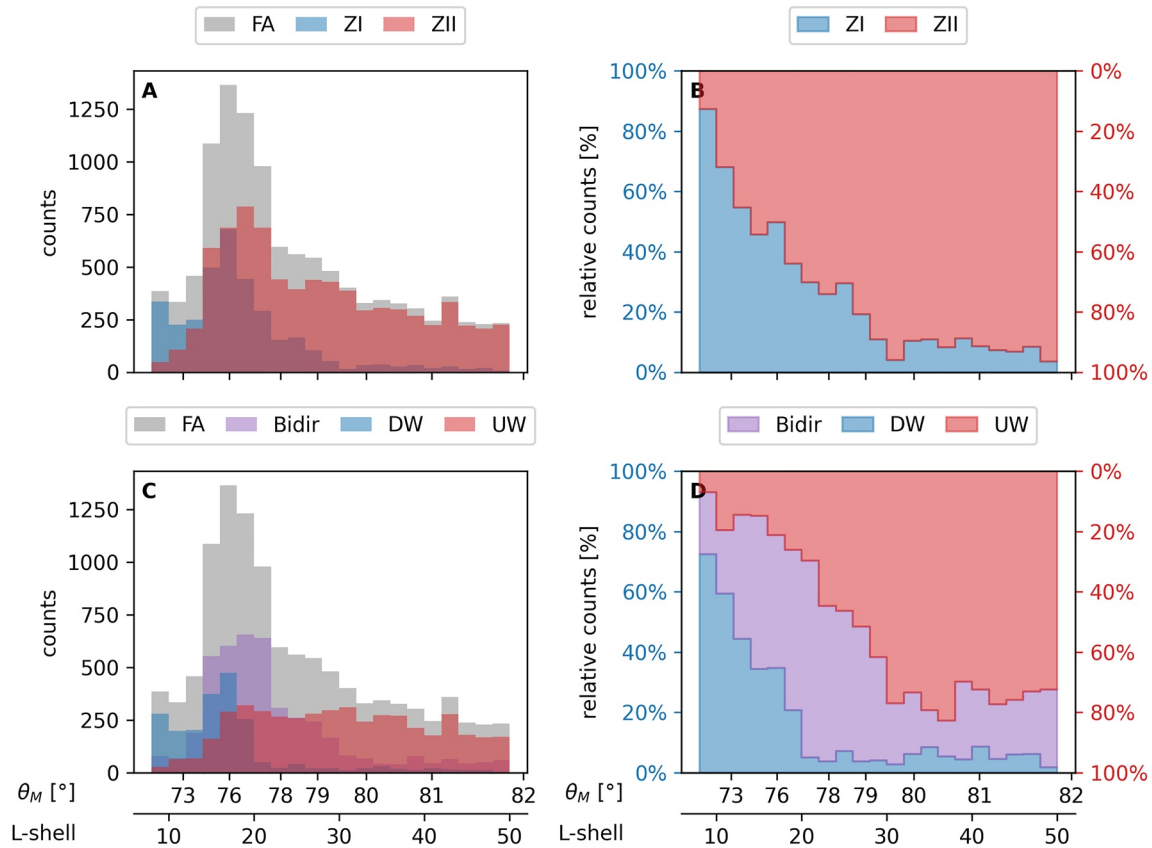
**Figure 7.** Histogram of Zone I (ZI) and Zone II (ZII), as well as upward (UW), downward (DW), and bidirectional distributions (Bidir), for field-aligned particles as a function of the magnetic latitude, distributed/organized by the dipole L-shell. Parts (a) and (c) show the absolute counts of classified distributions for the corresponding magnetic latitude. The stacked histogram (gray) of both parts shows the absolute counts of observations, where one count resembles one 0.5 s measurement. Parts (b) and (d) show the counts relative to the total number of observed distributions.

Similarly, we compare the energy fluxes between the mono-energetic and the broad-band distributions. First we consider the energy flux contributions from individual events. We find that individual mono-energetic structures provide on average slightly larger energy fluxes, that is, $R_{individual} = 1.43 \pm 0.52$ times larger than broadband events. It seems possible that the average energy flux of mono-energetic structures is overestimated by their nature, as they are only prominent when peaking with higher intensities than the background broadband intensities supplying only high-intensity data to the statistics. However, mono-energetic structures are much less frequently observed than broadband distributions and only contribute an overall energy flux of $10.7\% \pm 5.9\%$ (see Figures 6d and 6d). This implies that the energy flux of broadband distributions contributing to the main aurora is $R_{abs} = 8.36 \pm 4.73$ times higher (see Figure 6d). Therefore, we find that Jupiter's main auroral emissions are primarily produced via precipitating broadband electron distributions.

The classification of pitch angle distributions can be used to study another class of field-aligned distributions into two Zones, introduced by Mauk et al. (2020). Zone I defines the region of dominating downward energy fluxes with $F_{DW} > F_{UW}$ and Zone II where the dominating energy fluxes are upward, with $F_{UW} > F_{DW}$. Mauk et al. (2020) states that Zone I tend to occur at intermediate latitudes characteristic for an active downward acceleration process. Zone II tends to occur at high latitudes and is associated with an upward acceleration process. Bidirectionality in this zone is possible due to downward energy fluxes originating from an upward acceleration process in the opposing hemisphere Mauk et al. (2020). The occurrence of both zones in dependency on the magnetic latitude for field-aligned particles distributions is shown in Figures 7a and 7b. Both zones are present over the whole magnetic latitude range. Zone I has a high occurrence at small magnetic latitudes of less than $78°$, whereas zone II dominates the higher magnetic latitudes. A maximum occurrence of zone II is given around $\theta_M = 80°$. Figures 7c and 7d show that bidirectionality is dominating the intermediate magnetic latitudes centered around $\theta = 76°$. All four plots show a region dominated by downward energy fluxes for small magnetic latitudes.

**Table 1**
*Summary of Relative Occurrence of the Analyzed Distribution Functions*

|  | Field-aligned | Pancake | SD |
|---|---|---|---|
| $\theta_M > 76°$ | 87.6% | 13.8% | 7.2% |
| $\theta_M < 76°$ | 12.4% | 86.2% | 9.6% |
|  | Mono-energetic | Broadband | SD |
| Field-aligned | 7.0% | 93.0% | 3.8% |

*Note.* Pitch angular distributions are compared within two intervals separated at the 76° magnetic latitude corresponding to a dipole L-shell of 17.

One may speak of three regions, the first one dominated by downward flux, followed by a mostly bidirectional region, and one region at high magnetic latitudes with strong upward energy fluxes.

## 4. Discussion

This statistical study is based on JEDI measurements located over the main emission zone, with a radial distance of 1.2–2.5 $R_J$ and dipole L-shell between 8 and 50. Further restrictions follow from appropriate pitch-angle coverage and sufficient signal-to-noise ratio larger than three. Hence, the first 20 Juno flybys enable a total observation length of 358 min in the northern hemisphere and 165 min in the southern hemisphere. An overview of the different occurrences resulting from the classification scheme is summarized in Table 1.

The classification via pitch angle distributions showed that field-aligned distributions dominate with a mean fraction of 87.6% ± 7.2% over magnetic latitudes between 76° and 82°. Pancake distributions have a little contribution of 13.8% within the higher magnetic latitudes but strongly contribute by 86.2% ± 9.6% within small magnetic latitudes of less than 76°. Sixty-three percent of the pancake distributed measurements provide a larger energy flux in the downward direction compared to the upward direction and thus, are associated with diffuse aurora. Pancake distributions with dominating upward energy flux are embedded in low energy flux regions, where downward and upward energy fluxes are equally small. Our statistics showed that pancake distributions are likelier at smaller dipole L-shells, confirming expectations from diffuse aurora.

The classification via energy spectra showed that broadband distributions observed account for 93.0% ± 3.8% of the measurements averaged over all observed dipole L-shells, clearly dominating the field-aligned distributions. Mono-energetic structures are rarely observed with a total amount of 7.0% ± 3.8% averaged over all dipole L-shells, with no clear preference to particular spatial parameters, such as radial distance or magnetic latitude. Most of the identified mono-energetic structures were observed when the background broadband intensities were small. Some mono-energetic structures showed only small deviations from strong background intensities indicating a broadband distribution. It thus appears that some mono-energetic structures possess smaller intensities than broadband structures and are therefore hard to distinguish within strong background broadband distribution. The rate of mono-energetic structures may therefore be underestimated, but the contribution of mono-energetic structures to auroral acceleration may still be comparable due to the small intensities. Broadband distributions, though, are also somewhat underestimated as a superposition of broadband and mono-energetic distributions is classified as a mono-energetic distribution.

The classification via pitch angle distributions also offered an overview of dominating flux in the upward and downward directions. The statistics showed that dominating downward energy fluxes often occur at small magnetic latitudes, whereas upward energy fluxes are dominant within higher magnetic latitudes. A transition between both regions occurs in presence of bidirectional distributions, which dominate the magnetic latitudes from 74° up to 79°. These results confirm the observations made by Mauk et al. (2020) that downward electron acceleration mainly occurs at intermediate latitudes, whereas upward electron acceleration mainly occurs at high latitudes, possibly originating from upward and downward current regions, respectively. This conclusion partly explains the bidirectional pitch angle distributions, resulting from upward electron acceleration from both hemispheres. We summarize our findings in the following list:

1. Two zones are observed, separated at magnetic latitude 76°, where field-aligned distributions are prominent at higher magnetic latitudes and pancake distributions at smaller magnetic latitudes, indicating diffuse aurora.
2. Our statistic shows a dominant occurrence of broadband distributions, rather than mono-energetic structures which were rarely observed with a total amount of 7.0% averaged over all dipole L-shells within 8 and 50. No clear preference to particular spatial parameters could be observed.
3. A transition takes place, where dominating downward energy fluxes at small magnetic latitudes interchange through a bidirectional zone with dominating upward energy flux with higher magnetic latitudes, affirming observations made by Mauk et al. (2020).

4. Bidirectionality is a persistent pitch angle distributions property throughout the high magnetic latitudes and therefore suggests rather a bidirectional acceleration process than an upward acceleration from both hemispheres.

Our observed results might not fully represent the real statistical distribution because of the observational bias by the spatial coverage and restrictions of Juno's flybys. Field-aligned distributions are strongly dominated by broadband energy spectra with a contribution of 93.0%. Comparison of mean energy flux statistics with the count statistics showed similar results. Although broadband and mono-energetic distributions have comparable energy fluxes, mono-energetic distributions contribute little to the total amount of energy flux compared to broadband distributions and do not provide the main energy flux to the main emission zone.

The type of energy distribution gives information about the acceleration processes of the particles. Mono-energetic distributions usually result from electrostatic potentials, whereas broadband distributions result from stochastic acceleration processes. The presented statistic therefore contribute to the discussion about possible and probable acceleration processes and theories about the generation processes of Jupiter's aurora and most importantly to a quantitative contribution of the associated acceleration processes. The dominant occurrence of broadband distributions, within our statistics, supports the theory of a stochastic acceleration process as the dominant auroral driver. Mono-energetic structures are rarely observed, additionally, neither over a great amount of time or spatial sizes nor with a strong energy flux contribution.

These findings identified a mono-energetic distribution occurrence of 7.0%, which does not match the expectations prior to the Juno mission. A static current system as the dominant auroral driver, accelerating particles along with electrostatic potentials as introduced by Knight (1973), does not seem to be the dominant acceleration process for the electrons observed by Juno. The average occurrence of broadband distribution with more than 90% over the observed times does not suit the classic image but underlines the importance of a turbulent or stochastic acceleration process (e.g., Damiano et al., 2018; Elliott, Gurnett, Kurth, Mauk, et al., 2018; Lysak et al., 2021; Saur et al., 2018), as the dominant driver of the unique Jovian aurora.

## Abbreviations

| | |
|---|---|
| JEDI | Jupiter Energetic-particle Detector Instrument |
| JADE | Jovian Auroral Distributions Experiment |
| UVS | Ultraviolet Spectrograph |
| PJ | perijove |
| SSD | Solid state detector |
| LC | loss cone |
| FA | field-aligned |
| PA | pitch angle |
| SNR | signal-to-noise ratio |
| DifA | Diffuse aurora |
| ZI | Zone I |
| ZII | Zone II |
| HST | Hubble Space Telescope |
| JRM09 | Juno Reference Model through Perijove 9 |

## Data Availability Statement

Bagenal et al. (2017) was used as a reference to the utilized coordination systems (https://lasp.colorado.edu/home/mop/files/2015/02/CoOrd_systems7.pdf). The Juno-JEDI data were obtained from the website of the NASA Planetary Data System:Planetary Plasma Interactions (https://pds-ppi.igpp.ucla.edu/mission/JUNO/JNO/JEDI). Juno footprints data using JRM09 and CAN models is available at https://lasp.colorado.edu/home/mop/files/2020/04/20190412_Imai_MagFootReader_UIowa_rev.pdf. The classification results of this study are listed in Table S1 in Supporting Information S1.

# References

Allegrini, F., Bagenal, F., Bolton, S., Connerney, J., Clark, G., Ebert, R. W., et al. (2017). Electron beams and loss cones in the auroral regions of Jupiter. *Geophysical Research Letters*, *44*(14), 7131–7139. https://doi.org/10.1002/2017gl073180

Bagenal, F., Adriani, A., Allegrini, F., Bolton, S. J., Bonfond, B., Bunce, E. J., et al. (2017). Magnetospheric science objectives of the Juno mission. *Space Science Reviews*, *213*(1), 219–287. https://doi.org/10.1007/s11214-014-0036-8

Bagenal, F., & Delamere, P. A. (2011). Flow of mass and energy in the magnetospheres of Jupiter and Saturn. *Journal of Geophysical Research: Space Physics*, *116*(A5). https://doi.org/10.1029/2010ja016294

Baumjohann, W., & Treumann, R. A. (1997). *Basic space plasma physics*. Imperial College Press and. distributed by world scientific publishing co. https://doi.org/10.1142/p015

Bevington, P. R., Robinson, D. K., Blair, J. M., Mallinckrodt, A. J., & McKay, S. (1993). Data reduction and error analysis for the physical sciences. *Computers in Physics*, *7*(4), 415–416. https://doi.org/10.1063/1.4823194

Bolton, S. J., Lunine, J., Stevenson, D., Connerney, J. E. P., Levin, S., Owen, T. C., et al. (2017). The Juno mission. *Space Science Reviews*, *213*(1–4), 5–37. https://doi.org/10.1007/s11214-017-0429-6

Bonfond, B. (2012). When moons create aurora: The satellite footprints on giant planets. In *Auroral phenomenology and magnetospheric processes: Earth and other planets* (pp. 133–140). American Geophysical Union (AGU). https://doi.org/10.1029/2011GM001169

Clark, G., Mauk, B. H., Haggerty, D., Paranicas, C., Kollmann, P., Rymer, A., et al. (2017). Energetic particle signatures of magnetic field-aligned potentials over Jupiter's polar regions. *Geophysical Research Letters*, *44*(17), 8703–8711. https://doi.org/10.1002/2017gl074366

Clark, G., Mauk, B. H., Paranicas, C., Haggerty, D., Kollmann, P., Rymer, A., et al. (2017). Observation and interpretation of energetic ion conics in Jupiter's polar magnetosphere. *Geophysical Research Letters*, *44*(10), 4419–4425. https://doi.org/10.1002/2016gl072325

Clark, G., Tao, C., Mauk, B. H., Nichols, J., Saur, J., Bunce, E. J., et al. (2018). Precipitating electron energy flux and characteristic energies in Jupiter's main auroral region as measured by Juno/Jedi. *Journal of Geophysical Research: Space Physics*, *123*(9), 7554–7567. https://doi.org/10.1029/2018ja025639

Clarke, J. T., Ajello, J., Ballester, G., Ben Jaffel, L., Connerney, J., Gérard, J.-C., et al. (2002). Ultraviolet emissions from the magnetic footprints of IO, Ganymede and Europa on Jupiter. *Nature*, *415*(6875), 997–1000. https://doi.org/10.1038/415997a

Connerney, J. E. P., Acuna, M. H., & Ness, N. F. (1981). Modeling the Jovian current sheet and inner magnetosphere. *Journal of Geophysical Research*, *86*(A10), 8370–8384. https://doi.org/10.1029/ja086ia10p08370

Connerney, J. E. P., Adriani, A., Allegrini, F., Bagenal, F., Bolton, S. J., Bonfond, B., et al. (2017). Jupiter's magnetosphere and aurorae observed by the juno spacecraft during its first polar orbits. *Science*, *356*(6340), 826–832. https://doi.org/10.1126/science.aam5928

Connerney, J. E. P., Kotsiaros, S., Oliversen, R. J., Espley, J. R., Joergensen, J. L., Joergensen, P. S., et al. (2018). A new model of Jupiter's magnetic field from Juno's first nine orbits. *Geophysical Research Letters*, *45*(6), 2590–2596. https://doi.org/10.1002/2018gl077312

Cowley, S., & Bunce, E. (2001). Origin of the main auroral oval in Jupiter's coupled magnetosphere–ionosphere system. *Planetary and Space Science*, *49*(10), 1067–1088. https://doi.org/10.1016/s0032-0633(00)00167-7

Damiano, P., Chaston, C., Hull, A., & Johnson, J. (2018). Electron distributions in kinetic scale field line resonances: A comparison of simulations and observations. *Geophysical Research Letters*, *45*(12), 5826–5835. https://doi.org/10.1029/2018gl077748

Ebert, R. W., Allegrini, F., Bagenal, F., Bolton, S. J., Connerney, J. E. P., Clark, G., et al. (2017). Spatial distribution and properties of 0.1-100 keV electrons in Jupiter's polar auroral region. *Geophysical Research Letters*, *44*(18), 9199–9207. https://doi.org/10.1002/2017gl075106

Ebert, R. W., Greathouse, T. K., Clark, G., Allegrini, F., Bagenal, F., Bolton, S. J., et al. (2019). Comparing electron energetics and UV brightness in Jupiter's northern polar region during Juno perijove 5. *Geophysical Research Letters*, *46*(1), 19–27. https://doi.org/10.1029/2018gl081129

Elliott, S. S., Gurnett, D. A., Kurth, W. S., Clark, G., Mauk, B. H., Bolton, S. J., et al. (2018). Pitch angle scattering of upgoing electron beams in Jupiter's polar regions by whistler mode waves. *Geophysical Research Letters*, *45*(3), 1246–1252. https://doi.org/10.1002/2017gl076878

Elliott, S. S., Gurnett, D. A., Kurth, W. S., Mauk, B. H., Ebert, R. W., Clark, G., et al. (2018). The acceleration of electrons to high energies over the Jovian polar cap via whistler mode wave-particle interactions. *Geophysical Research Letters*, *123*(9), 7523–7533. https://doi.org/10.1029/2018ja025797

Gérard, J.-C., Bonfond, B., Grodent, D., Radioti, A., Clarke, J. T., Gladstone, G. R., et al. (2014). Mapping the electron energy in Jupiter's aurora: Hubble spectral observations. *Journal of Geophysical Research: Space Physics*, *119*(11), 9072–9088. https://doi.org/10.1002/2014ja020514

Gérard, J.-C., Bonfond, B., Mauk, B. H., Gladstone, G. R., Yao, Z. H., Greathouse, T. K., et al. (2019). Contemporaneous observations of Jovian energetic auroral electrons and ultraviolet emissions by the Juno spacecraft. *Journal of Geophysical Research: Space Physics*, *124*(11), 8298–8317. https://doi.org/10.1029/2019ja026862

Grodent, D., Bonfond, B., Yao, Z., Gérard, J.-C., Radioti, A., Dumont, M., et al. (2018). Jupiter's aurora observed with HST during Juno orbits 3 to 7. *Journal of Geophysical Research: Space Physics*, *123*(5), 3299–3319. https://doi.org/10.1002/2017ja025046

Hill, T. W. (1979). Inertial limit on corotation. *Journal of Geophysical Research: Space Physics*, *84*(A11), 6554–6558. https://doi.org/10.1029/ja084ia11p06554

Hill, T. W. (2001). The Jovian auroral oval. *Journal of Geophysical Research: Space Physics*, *106*(A5), 8101–8107. https://doi.org/10.1029/2000ja000302

Kimura, T., Badman, S. V., Tao, C., Yoshioka, K., Murakami, G., Yamazaki, A., et al. (2015). Transient internally driven aurora at Jupiter discovered by Hisaki and the Hubble space telescope. *Geophysical Research Letters*, *42*(6), 1662–1668. https://doi.org/10.1002/2015gl063272

Knight, S. (1973). Parallel electric fields. *Planetary and Space Science*, *21*(5), 741–750. https://doi.org/10.1016/0032-0633(73)90093-7

Kotsiaros, S., Connerney, J. E. P., Clark, G., Allegrini, F., Gladstone, G. R., Kurth, W. S., et al. (2019). Birkeland currents in Jupiter's magnetosphere observed by the polar-orbiting Juno spacecraft. *Nature Astronomy*, *3*(10), 904–909. https://doi.org/10.1038/s41550-019-0819-7

Kurth, W. S., Mauk, B. H., Elliott, S. S., Gurnett, D. A., Hospodarsky, G. B., Santolik, O., et al. (2018). Whistler mode waves associated with broadband auroral electron precipitation at jupiter. *Geophysical Research Letters*, *45*(18), 9372–9379. https://doi.org/10.1029/2018gl078566

Li, W., Thorne, R. M., Ma, Q., Zhang, X.-J., Gladstone, G. R., Hue, V., et al. (2017). Understanding the origin of Jupiter's diffuse aurora using Juno's first perijove observations. *Geophysical Research Letters*, *44*(20), 10162–10170. https://doi.org/10.1002/2017gl075545

Lysak, R. L., Song, Y., Elliott, S., Kurth, W., Sulaiman, A. H., & Gershman, D. (2021). The Jovian ionospheric Alfvén resonator and auroral particle acceleration. *Journal of Geophysical Research: Space Physics*, e2021JA029886. https://doi.org/10.1029/2021JA029886

Mauk, B. H., & Bagenal, F. (2012). Comparative auroral physics: Earth and other planets. In *Auroral phenomenology and magnetospheric processes: Earth and other planets* (pp. 3–26). American Geophysical Union (AGU). https://doi.org/10.1029/2011GM001192

Mauk, B. H., Clark, G., Gladstone, G. R., Kotsiaros, S., Adriani, A., Allegrini, F., et al. (2020). Energetic particles and acceleration regions over Jupiter's polar cap and main aurora: A broad overview. *Journal of Geophysical Research: Space Physics*, *125*(3). https://doi.org/10.1029/2019ja027699

Mauk, B. H., Clarke, J. T., Grodent, D., Waite, J. H., Paranicas, C. P., & Williams, D. J. (2002). Transient aurora on Jupiter from injections of magnetospheric electrons. *Nature*, *415*(6875), 1003–1005. https://doi.org/10.1038/4151003a

Mauk, B. H., Haggerty, D. K., Jaskulek, S. E., Schlemm, C. E., Brown, L. E., Cooper, S. A., et al. (2017). The Jupiter energetic particle detector instrument (jedi) investigation for the Juno mission. *Space Science Reviews*, *213*(1), 289–346. https://doi.org/10.1007/s11214-013-0025-3

Mauk, B. H., Haggerty, D. K., Paranicas, C., Clark, G., Kollmann, P., Rymer, A. M., et al. (2017a). Juno observations of energetic charged particles over Jupiter's polar regions: Analysis of monodirectional and bidirectional electron beams. *Geophysical Research Letters*, *44*(10), 4410–4418. https://doi.org/10.1002/2016gl072286

Mauk, B. H., Haggerty, D. K., Paranicas, C., Clark, G., Kollmann, P., Rymer, A. M., et al. (2017b). Discrete and broadband electron acceleration in Jupiter's powerful aurora. *Nature*, *549*(7670), 66–69. https://doi.org/10.1038/nature23648

Mauk, B. H., Haggerty, D. K., Paranicas, C., Clark, G., Kollmann, P., Rymer, A. M., et al. (2018). Diverse electron and ion acceleration characteristics observed over Jupiter's main aurora. *Geophysical Research Letters*, *45*(3), 1277–1285. https://doi.org/10.1002/2017gl076901

Mauk, B. H., & Saur, J. (2007). Equatorial electron beams and auroral structuring at Jupiter. *Journal of Geophysical Research: Space Physics*, *112*(A10). https://doi.org/10.1029/2007ja012370

McComas, D. J., Alexander, N., Allegrini, F., Bagenal, F., Beebe, C., Clark, G., et al. (2017). The Jovian auroral distributions experiment (JADE) on the Juno mission to Jupiter. *Space Science Reviews*, *213*(1–4), 547–643. https://doi.org/10.1007/s11214-013-9990-9

Newell, P. T., Sotirelis, T., & Wing, S. (2009). Diffuse, monoenergetic, and broadband aurora: The global precipitation budget. *Journal of Geophysical Research: Space Physics*, *114*(A9). https://doi.org/10.1029/2009ja014326

Ni, B., Thorne, R. M., Zhang, X., Bortnik, J., Pu, Z., Xie, L., et al. (2016). Origins of the earth's diffuse auroral precipitation. *Space Science Reviews*, *200*(1), 205–259. https://doi.org/10.1007/s11214-016-0234-7

Nichols, J. D., & Cowley, S. W. H. (2004). Magnetosphere-ionosphere coupling currents in Jupiter's middle magnetosphere: Effect of precipitation-induced enhancement of the ionospheric pedersen conductivity. *Annales Geophysica*e, *22*(5), 1799–1827. https://doi.org/10.5194/angeo-22-1799-2004

Ray, L. C., Ergun, R. E., Delamere, P. A., & Bagenal, F. (2010). Magnetosphere-ionosphere coupling at Jupiter: Effect of field-aligned potentials on angular momentum transport. *Journal of Geophysical Research: Space Physics*, *115*(A9). https://doi.org/10.1029/2010ja015423

Saur, J., Janser, S., Schreiner, A., Clark, G., Mauk, B. H., Kollmann, P., et al. (2018). Wave-particle interaction of Alfvén waves in Jupiter's magnetosphere: Auroral and magnetospheric particle acceleration. *Journal of Geophysical Research: Space Physics*, *123*(11), 9560–9573. https://doi.org/10.1029/2018ja025948

Saur, J., Mauk, B. H., Mitchell, D. G., Krupp, N., Khurana, K. K., Livi, S., et al. (2006). Anti-planetward auroral electron beams at Saturn. *Nature*, *439*(7077), 699–702. https://doi.org/10.1038/nature04401

Saur, J., Pouquet, A., & Matthaeus, W. H. (2003). An acceleration mechanism for the generation of the main auroral oval on Jupiter. *Geophysical Research Letters*, *30*(5). https://doi.org/10.1029/2003gl017730

Seiff, A., Kirk, D. B., Knight, T. C. D., Young, R. E., Mihalov, J. D., Young, L. A., et al. (1998). Thermal structure of Jupiter's atmosphere near the edge of a 5-μm hot spot in the north equatorial belt. *Journal of Geophysical Research: Planets*, *103*(E10), 22857–22889. https://doi.org/10.1029/98je01766

Szalay, J. R., Allegrini, F., Bagenal, F., Bolton, S. J., Clark, G., Connerney, J. E. P., et al. (2021). Proton outflow associated with Jupiter's auroral processes. *Geophysical Research Letters*, *48*(1), e2020GL091627. https://doi.org/10.1029/2020gl091627

Tao, C., Kimura, T., Badman, S. V., André, N., Tsuchiya, F., Murakami, G., et al. (2015). Variation of Jupiter's aurora observed by Hisaki/exceed: 2. Estimations of auroral parameters and magnetospheric dynamics. *Journal of Geophysical Research: Space Physics*, *121*(5), 4055–4071. https://doi.org/10.1002/2015JA021272

Tetrick, S. S., Gurnett, D. A., Kurth, W. S., Imai, M., Hospodarsky, G. B., Bolton, S. J., et al. (2017). Plasma waves in Jupiter's high-latitude regions: Observations from the Juno spacecraft. *Geophysical Research Letters*, *44*(10), 4447–4454. https://doi.org/10.1002/2017gl073073